Experimental and Theoretical Studies of the Reaction of Rh^+ with CS_2 in the Gas Phase: Thermochemistry of RhS^+ and $RhCS^+$

P. B. Armentrout*

Department of Chemistry, University of Utah, 314 S. 1400 E., Rm 2020, Salt Lake City, Utah, 84112

Ilona Kretzschmar

Department of Chemical Engineering, The City College of New York, New York, New York 10031

Received: July 29, 2009; Revised Manuscript Received: August 24, 2009

The gas-phase reactivity of the atomic transition-metal cation rhodium, Rh^+, with CS_2 is investigated using guided-ion-beam mass spectrometry (GIBMS). Endothermic reactions forming RhS^+ and $RhCS^+$ are observed. Analysis of the kinetic energy dependence of the cross sections for formation of these two products yields the 0 K bond energies of $D_0(Rh^+-S) = 2.61 \pm 0.12$ eV and $D_0(Rh^+-CS) = 2.66 \pm 0.19$ eV. These compare favorably with quantum chemical calculations at the CCSD(T)/Def2TZVPP//B3LYP/Def2TZVPP and CCSD(T)/Def2TZVPP levels of theory, where the former is also used to explore the complete potential energy surface of the reaction. It is found that the reaction initially involves insertion of the rhodium cation into one of the CS bonds of CS_2, followed by metal ligand cleavages to form the two product channels. The formation of ground state RhS^+ products is spin-forbidden, whereas $RhCS^+$ formation is spin-allowed. Crossing points between the triplet and quintet surfaces are located in the region of the $SRh^+(CS)$ intermediate, which suggests that coupling between the surfaces is reasonably efficient, consistent with experiment.

Introduction

Second-row transition-metal sulfides show high activity in industrially relevant hydrotreating processes.[1−3] Rhodium sulfide in particular is the most active transition-metal sulfide catalyst in the hydrodenitrogenation of quinoline,[4] but it is second in activity to ruthenium sulfide in hydrotreatment of coal-derived naphtha.[2] The latter finding has led to the suggestion that a combination of rhodium and ruthenium in a ternary transition-metal sulfide[5] could be of advantage for hydrotreating catalysis. Interestingly, the intermediate Rh−S bond energy makes rhodium sulfide the most active catalyst in the transformation of 2,3-dimethylbut-2-ene, a model gasoline olefin.[6] It also enables rhodium sulfide to reduce the nitro group in bis(4-nitrophenyl) sulfide without hydrogenolysis of the thioether linkage.[7] Further, rhodium sulfide has been found to enable synthesis of methanol from CO and H_2 in the presence of H_2S.[8] More recently, rhodium sulfide has received interest as an electrocatalyst in the oxygen reduction reaction, a process important for the depolarized electrolysis of hydrochloric acid used industrially for the recovery of chlorine.[9,10] The requirement for a uniform distribution of the rhodium sulfide catalyst and the stability of the carbon support has led to the synthesis of highly dispersed rhodium nanoparticles on carbon nanotubes.[11] Rhodium sulfide nanoparticles have also been synthesized by hydro-[12] and solvothermal methods.[13] Further, synthesis of rod-shaped Rh_2S_3 nanoparticles via thermolyzation of a rhodium metal−organic complex and the growth of Rh_2S_3 films from the same complex have been reported.[14] Formation of a rhodium sulfide layer on cadmium sulfide yields an active photocatalyst for photochemical decomposition of aqueous sulfides.[15] Interestingly, rhodium sulfide has served historically as a vehicle to remove rhodium from other platinum-group metals.[16,17] It has also been used as a matrix for removal of Au, Ag, Pt, and Pd from geological samples.[18]

Despite the increasing interest in the use of rhodium sulfide as a catalyst in many industrial processes, the intrinsic function, structure, and thermodynamic properties of rhodium sulfide have been scarcely studied and are not yet fully understood. With the exception of a spectroscopic analysis of jet-cooled rhodium monosulfide, RhS,[19] there is very little thermodynamic or spectroscopic data available for rhodium sulfides. In previous work, we have investigated the gas-phase thermodynamic properties of the sulfides of first-row[20−28] and several early second-row[28,29] transition-metal cations, as well as reviewed the periodic trends in this information.[30] In the present work, we extend our studies to one of the late metals of the second transition row, i.e., rhodium, which complements work on ruthenium, palladium, and silver.[31−33] The reactions of the atomic cations of this element with carbon disulfide, CS_2, are studied using guided-ion-beam mass spectrometric (GIBMS) techniques. Reactions 1 and 2 are both observed and their dependence on kinetic energy is measured.

$$Rh^+ + CS_2 \rightarrow RhS^+ + CS \quad (1)$$

$$\rightarrow RhCS^+ + S \quad (2)$$

An analysis of this kinetic energy dependence permits the endothermicities of these reactions to be measured and converted to the 0 K bond dissociation energies, $D_0(Rh^+-S)$ and $D_0(Rh^+-CS)$. Quantum chemical methods are employed to complement the thermodynamic data with information on electronic ground and low-lying excited states, bond lengths, and vibrational frequencies of RhS^+ and $RhCS^+$. The quantum

* To whom correspondence should be addressed. E-mail: armentrout@chem.utah.edu.

10.1021/jp907253r CCC: $40.75
Published on Web 09/18/2009

chemical methods are also used to examine the potential energy surface for reaction, revealing insight into the reaction mechanism.

Methods

Experimental Section. GIB mass spectrometry is used for the evaluation of thermodynamic data by means of threshold measurements of endothermic reactions. Detailed descriptions of the guided-ion-beam apparatus used in this study and the experimental procedures are given elsewhere.[34,35] Briefly, Ar^+ ions created in a dc discharge source[35] are accelerated toward a rhodium cathode, thereby sputtering off Rh^+ ions. The metal ions drift in a meter-long flow tube operated with a 9:1 mixture of helium and argon at a pressure of ~90 Pa. The ions undergo $\sim 10^5$ collisions with the buffer gas before exiting the flow tube. In previous work, reactions of rhodium cations produced using the flow tube source and those created by surface ionization at 2200 K were compared.[36] This work suggested that the temperature of the ions formed in the flow tube source is <1100 K. Further studies of Rh^+ with O_2[37] and alkanes[38,39] also found no evidence for excited states, and none were found in the present study either.

Following extraction from the source, the ions are accelerated and focused into a magnetic sector, mass-selected, decelerated to a desired kinetic energy, and focused into an octopole ion trap.[34,40] This device guides the ions through a static gas cell kept at a low pressure (~0.007−0.013 Pa) of the reactant gas. It was verified that all product cross sections reported result from single ion−molecule collisions by examining the pressure dependence of the product intensities. After exiting the gas cell, product and unreacted beam ions drift to the end of the octopole, where they are directed into a quadrupole mass filter for mass analysis and then detected. Conversion of the raw ion intensities into reaction cross sections and the conversion from the laboratory to center-of-mass energy scale are treated as described previously.[34] The accuracy of the absolute cross sections is estimated to be ±20%. A retarding technique is used to determine the ion energy distribution and absolute zero of the energy scale.[34] The beams have Gaussian kinetic energy distributions with average full widths at half-maximum (fwhm) of ca. 0.25 eV in the laboratory frame. The uncertainty of the absolute energy scale is ±0.05 eV (lab).

Quantitative analysis of the energy dependence of these cross sections is achieved using eq 3 and methods outlined elsewhere.[41−45]

$$\sigma(E) = \sigma_0 \sum g_i (E + E_i - E_0)^n / E^m \qquad (3)$$

In eq 3, E is the relative kinetic energy of the reactants, E_0 is the threshold for reaction at 0 K, σ_0 is a scaling parameter, and n and m (which is usually set to unity) are fitting parameters that describe the energy dependence of the reaction. The summation is over the rovibrational states of the reactants having energies E_i and populations g_i ($\sum g_i = 1$), with molecular parameters for CS_2 taken from B3LYP/Def2TZVPP calculations performed here for consistency. (Vibrational frequencies agree with experiment[46] within 3% and the rotational constants are the same.)

In addition to modeling the reaction product cross sections independently using eq 3, we also examine competition between the two product channels and a return to reactants by using a statistical approach that has been described in detail elsewhere,[47,48] eq 4.

$$\sigma_j(E) = (n\sigma_{0,j}/E^m) \sum g_i \int_{E_{0,j}-E_i}^{E} [k_j(E^*)/k_{tot}(E^*)] \times [1 - e^{k_{tot}(E^*)\tau}](E - \varepsilon)^{n-1}\, d(\varepsilon) \qquad (4)$$

Here $\sigma_{0,j}$ is an adjustable scaling parameter for channel j that is energy independent, $E_{0,j}$ represents the CID threshold energy for channel j at 0 K, ε is the energy available from reactant translation, and τ is the experimental time for dissociation. E^* is the internal energy of the energized molecule (EM), i.e., $E^* = \varepsilon + E_i$. The term $k_j(E^*)$ is the unimolecular rate constant for dissociation of the EM to channel j. The rate constants $k_j(E^*)$ and $k_{tot}(E^*)$ are defined by Rice−Ramsperger−Kassel−Marcus (RRKM)[49−51] theory in eq 5,

$$k_{tot}(E^*) = \sum k_j(E^*) = \sum d_j N^{\dagger}_{j,vr}(E^* - E_{0,j})/h\rho_{vr}(E^*) \qquad (5)$$

where d_j is the reaction degeneracy for channel j, h is Planck's constant, $N^{\dagger}_{j,vr}(E^* - E_{0,j})$ is the sum of rovibrational states of the transition state (TS) at an energy $E^* - E_{0,j}$ for channel j, and $\rho_{vr}(E^*)$ is the density of rovibrational states of the EM at the available energy, E^*. Transition states for both reaction channels and the return to reactants are treated as loose transition states at the phase space limit (PSL),[47] in which case molecular parameters for the EM and TSs are taken from the quantum chemical calculations described below. Because reaction 2 corresponds to a covalent bond cleavage, we also considered whether a tight transition state might be more appropriate, as this has been found for other systems involving covalent bonds.[52,53] Here, the molecular parameters of the transition state are equated with those of the EM after removing the reaction coordinate, the Rh−S stretch. This is the tightest conceivable transition state for a bond cleavage reaction that has no barrier along the dissociation coordinate, as verified by quantum calculations for reaction 2.

Before comparison with the data, eqs 3 and 4 are convoluted over the translational energy distributions of both reactants. This determination of the reaction thresholds involves explicit consideration of the distributions of vibrational, rotational, and translational energies of both reactants. Because all sources of reactant energy are considered, the thermochemistry obtained corresponds to 0 K values in all cases.

Theoretical. The bond lengths and the ground state/excited state splittings of RhS^+ and $RhCS^+$ are calculated using density functional theory (DFT). Preliminary DFT calculations[30] were carried out using the Amsterdam density functional (ADF, version 2.0.1) suite of programs[54] with the inner-shell electrons ([Ne] for S and [Ar] for Rh) treated in the frozen-core approximation.[55] The valence orbitals are expanded as linear combinations of Slater-type basis functions. Triple-ζ basis sets are used for rhodium, carbon, and sulfur. All molecular and atomic energies are calculated using the local spin density approximation (LDA) with Slater's exchange functional and the Vosko−Wilk−Nusair (VWN) parametrization[56] augmented by Becke's[57] and Perdew's[58] (BP) gradient corrections for the exchange and correlation potentials, respectively.[59] This method will be referred to as ADF/BP. Particular advantages of the ADF program are that it provides control over the symmetry of the wave function created during geometry optimizations and permits the calculations of the excited states.

Using these geometries as starting point, we perform calculations using the Gaussian 03 suite of programs[60] with the B3LYP hybrid density functional method[61,62] and Def2TZVPP basis sets,

which are balanced basis sets of triple-ζ valence quality, with contracted basis functions of [5s3p2d1f] for C, [5s5p3d1f] for S, and [6s4p3d2f1g] for Rh.[63,64] The Def2TZVPP basis set for Rh uses a small core (28 electron) effective core potential (ECP) developed by Andrae et al.[65] These basis sets were obtained from the EMSL basis set library.[66,67] Geometries and relative energies found at this level of theory are comparable to those found for the ADF/BP level; hence, the latter results are not reported below because the ADF approach is not designed to yield accurate absolute energetics. In addition, to provide more accurate thermodynamic information, we also calculate single point energies of Rh^+, S, CS, CS_2, RhS^+, and $RhCS^+$ at the CCSD(T)/Def2TZVPP level of theory[68,69] using B3LYP/Def2TZVPP geometries and zero point energy corrections. The CCSD(T)/Def2TZVPP//B3LYP/Def2TZVPP level of theory is also used to examine the potential energy surfaces for the reactions. In all cases reported below, the single point energies cited include zero point energy corrections using unscaled B3LYP/Def2TZVPP vibrational frequencies. Finally, geometry optimizations at the CCD/Def2TZVPP (chosen because of the availability of analytic gradients) as well as CCSD(T)/Def2TZVPP levels are performed on the ground states of RhS^+ and $RhCS^+$ to examine the dependence of the structures on the level of theory. Because the results presented below generally involve only the Def2TZVPP basis set, they will usually be distinguished only by the level of theory used.

The thermodynamic accuracy of our calculated results can be assessed by comparing to several well-known experimental quantities. At the CCSD(T)/Def2TZVPP (B3LYP/Def2TZVPP) levels of theory, C−S and S−CS bond energies are calculated to be 7.05 (7.14) and 4.35 (4.70) eV, respectively. These values compare well with the experimental bond energies of 7.37 ± 0.04 and 4.50 ± 0.04 eV, respectively.[70] Likewise, the average excitation energies of different spin states of Rh^+ are reproduced reasonably well. Experiment finds a $^3F(4d^8)$ ground state for Rh^+, with a $^3P(4d^8)$ state at 0.94 eV (average over all spin−orbit levels of both states), a $^1D(4d^8)$ state at 1.24 eV, a $^1G(4d^8)$ state at 1.64 eV, and a $^5F(5s^14d^7)$ state at 1.99 eV.[71] The two levels of theory find a ^3F ground state and yield values of 2.08 (2.26) eV for the ^5F state excitation energy, in good agreement with experiment. Theoretical results for the singlet state depend on whether restricted or unrestricted calculations are done. At the restricted level, which yields an electronic configuration corresponding to a component of the ^1G state, excitation energies of 1.71 (1.99) eV are determined, in good agreement with experiment. For an unrestricted calculation, which would allow a configuration associated with the ^1D state, excitation energies of 0.51 (0.54) eV are obtained but are spin-contaminated, explaining why these values are much lower than the experimental excitation energy. Finally, we calculated the bond length and vibrational frequency for neutral $RhS(^4\Sigma^-)$ to compare with recent spectroscopic studies yielding $r(Rh-S) = 2.059$ Å and ~485 cm^{-1}.[19] The B3LYP/Def2TZVPP results are 2.066 Å and 491 cm^{-1}, in good agreement with the experimental values.

Theoretical Results

To fully understand the experimental results, it is important to know the nature of the electronic states of the product RhS^+ and $RhCS^+$ species, along with the potential energy surfaces for reaction. The following section contains the theoretical results as obtained using the computational procedures described above.

RhS^+. At the B3LYP/Def2TZVPP level of theory, calculations predict a $^5\Delta$ ground state for RhS^+ with higher lying triplet, singlet, and quintet excited states (Table 1). All of these states can dissociate adiabatically to the $Rh(^3F) + S(^3P)$ ground state asymptote. The ground state configuration is $(1\sigma)^2(2\sigma)^2(1\pi)^4(1\delta)^3(3\sigma)^1(2\pi)^2$, where the 1σ orbital is largely S(3s), the 2σ and 1π orbitals are the metal−sulfur bonding orbitals, the 1δ are Rh(4d), the 3σ is largely Rh(5s), and 2π and 4σ are antibonding orbitals. This state can be viewed as donation of the doubly occupied 3p orbital of S into the empty 5s orbital of $Rh^+(^3F,4d^8)$ with the electron holes in the $4d_\sigma$ and $4d_\delta$ orbitals. The bond lengths calculated at the B3LYP and CCD levels differ by 0.054 Å, and the result for CCSD(T) optimization agrees better with the B3LYP result (Table 1). Excited $^5\Sigma^+$ and $^5\Pi$ quintet states are found to lie 1.50 (1.51) and 2.02 (2.15) eV higher in energy at the CCSD(T) (B3LYP) levels of theory. These states have electron configurations of $(1\sigma)^2(2\sigma)^2(1\pi)^4(1\delta)^2(3\sigma)^2(2\pi)^2$ and $(1\sigma)^2(2\sigma)^2(1\pi)^4(1\delta)^2(3\sigma)^1(2\pi)^3$, corresponding to $1\delta \rightarrow 3\sigma$ and $1\delta \rightarrow 2\pi$ excitations, respectively. This suggests that the 3σ orbital has some antibonding character and clearly shows the antibonding character of the 2π orbital. The lowest excited state for RhS^+ is a $^3\Sigma^-$ having a $(1\sigma)^2(2\sigma)^2(1\pi)^4(1\delta)^4(3\sigma)^0(2\pi)^2$ configuration and lying only 0.34 (0.36) eV above the ground state (0.44 eV at the CCSD(T)/CCD level and 0.33 eV at the CCSD(T) level). Another triplet state, $^3\Pi$, lies 0.55 (0.52) eV above the ground state and has a $(1\sigma)^2(2\sigma)^2(1\pi)^4(1\delta)^4(3\sigma)^1(2\pi)^1$ configuration, again suggesting antibonding character in the 3σ orbital. Finally, a $^1\Sigma^+$ state lying 0.82 (1.26) eV above the ground state and having a $(1\sigma)^2(2\sigma)^2(1\pi)^4(1\delta)^4(3\sigma)^2(2\pi)^0$ configuration was also located. Bond lengths increase as the state multiplicity increases, which can be related to the occupation of the 3σ and 2π orbitals, where the 2π is more strongly antibonding. The CCD bond length for the excited $^5\Sigma^+$ state is again much longer than that calculated at the B3LYP level, with the CCSD(T)-optimized geometry again agreeing better with the latter (Table 1).

TABLE 1: State Splittings, Bond Lengths, and Vibrational Frequencies for RhS^+[a]

state	r, Å	ν, cm^{-1}	E_{rel}, eV[b]
$^5\Delta$	2.126, **2.180**, *2.106*	427, **303**	0.00 (0.00) **0.00**, *0.00*
$^3\Sigma^-$	2.033, **2.189**, *2.038*	528, **289**	0.34 (0.36) **0.44**, *0.33*
$^3\Pi$	2.010	497	0.55 (0.52)
$^1\Sigma^+$	1.980	557	0.82 (1.26)
$^5\Sigma^+$	2.228	361	1.50 (1.51)
$^5\Pi$	2.261	353	2.02 (2.15)

[a] Geometry optimizations and frequency calculations performed at the B3LYP/Def2TZVPP (CCD/Def2TZVPP in bold, CCSD(T)/Def2TZVPP in italics) level of theory. [b] Single point energies calculated at the CCSD(T)/Def2TZVPP (B3LYP/Def2TZVPP) levels of theory.

$RhCS^+$. The ground state of rhodium thiocarbonyl is calculated to be a $^3\Delta$ state corresponding to binding of CS to the ^3F ground state of Rh^+. As shown in Table 2, the CS bond length in this molecule is slightly shorter than in free CS, 1.509 versus 1.532 Å (1.478 versus 1.527 Å at the CCD level of theory, and 1.513 versus 1.544 Å at the CCSD(T) level of theory). Consistent with the change in bond length, the vibrational frequency of the CS bond stretch increases from 1311 to 1435 cm^{-1}. The $^3\Delta$ state has a valence electron configuration of $(1\sigma)^2(2\sigma)^2(1\pi)^4(3\sigma)^2(2\pi)^4(1\delta)^3(4\sigma)^1(3\pi)^0$, where the 1σ, 2σ, and 1π orbitals are the carbon−sulfur bonding orbitals, the 3σ is a metal−carbon bond formed by donation of the HOMO of CS into a 5s−4d hybrid on Rh, the 2π are the back-bonding interactions between the metal and the antibonding π orbitals on CS, the 1δ are Rh(4d), the 4σ is the other Rh(5s−4d)

TABLE 2: State Splittings, Geometries, and Vibrational Frequencies for $RhCS^+$[a]

species	state	r(M-C), Å	r(C−S), Å	∠MCS, deg	ν, cm^{-1}	E_{rel}, eV[b]
CS	$^1\Sigma^+$		1.532		1311	0.00 (0.00)
			1.527		**1362**	
			1.544			
$RhCS^+$	$^3\Delta$	1.896	1.509	180.0	260 (2), 347, 1435	0.00 (0.00)
		1.966	**1.478**	**180.0**		
		1.904	*1.513*	*180.0*		
	$^1\Sigma^+$	1.775	1.519	180.0	296 (2), 435, 1420	0.25 (0.38)
	$^5A''$	1.947	1.574	130.6	156, 424, 912	3.24 (3.10)

[a] Geometry optimizations and frequency calculations performed at the B3LYP/Def2TZVPP (CCD/Def2TZVPP in bold, CCSD(T)/Def2TZVPP in italics) level of theory. [b] Single point energies calculated at the CCSD(T)/Def2TZVPP (B3LYP/Def2TZVPP) levels of theory.

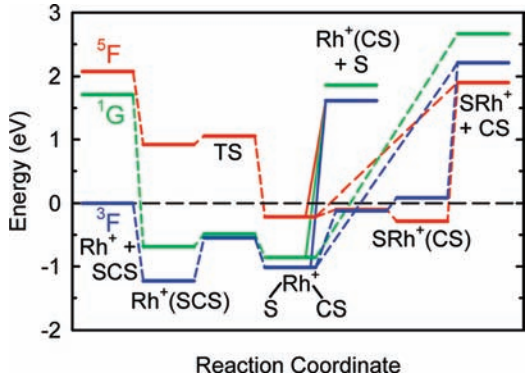

Figure 1. Reaction coordinate diagram for reaction of Rh^+ in triplet (blue line), singlet (green line), and quintet (red line) states with CS_2. All energies are calculated at the CCSD(T)//B3LYP level including zero point energies. Dissociation from linear $SRh^+(CS)$ to $Rh^+(CS)$ + S products is not explicitly shown.

hybrid, and the 3π and 4σ are Rh−C antibonding orbitals. The geometries calculated at the CCD level have a RhC bond that is 0.070 Å longer and a 0.031 Å shorter CS bond than results from the B3LYP geometries. CCSD(T) optimizations of this state yield results very close to the B3LYP results (Table 2). Calculations also find a low-lying singlet $^1\Sigma^+$ state, 0.25 (0.38) eV higher in energy, with a much shorter Rh−C bond length, 1.775 versus 1.896 Å. Here, the electron configuration is $(1\sigma)^2(2\sigma)^2(1\pi)^4(3\sigma)^2(2\pi)^4(1\delta)^4(4\sigma)^0(3\pi)^0$, which indicates that the 4σ has antibonding character. In contrast, a $^5A''$ state has a bent geometry with a much longer Rh−C bond length (1.947 Å) and a lower CS bond stretch (912 cm^{-1}). Using linear symmetry designations, this state has a $(1\sigma)^2(2\sigma)^2(1\pi)^4(3\sigma)^2(2\pi)^3(1\delta)^3(4\sigma)^1(3\pi)^1$ configuration in which one of the back-bonding 2π orbitals is singly occupied, which explains why the molecule is bent. The quintet species lies quite high in energy, 3.24 (3.10) eV above the $^3\Delta$ ground state, such that it is bound by only 1.52 (1.90) eV relative to the $Rh^+(^5F)$ + CS asymptote at the CCSD(T) (B3LYP) levels of theory. In contrast, the ground state is bound by 2.74 (2.99) eV. At the CCSD(T)/CCD and CCSD(T) levels of theory, the $^3\Delta$ ground state is calculated to be bound by 2.69 and 2.80 eV, respectively.

Potential Energy Surfaces. Figure 1 shows the reaction coordinate diagram for reaction of CS_2 with Rh^+ in the triplet, singlet, and quintet spin states. The energies used in this diagram are calculated at the CCSD(T)//B3LYP level of theory and are used throughout the following discussion. Geometries for the intermediates and products are shown in Figures 2, 3, and 4 for the triplet, singlet, and quintet surfaces, respectively. Relative

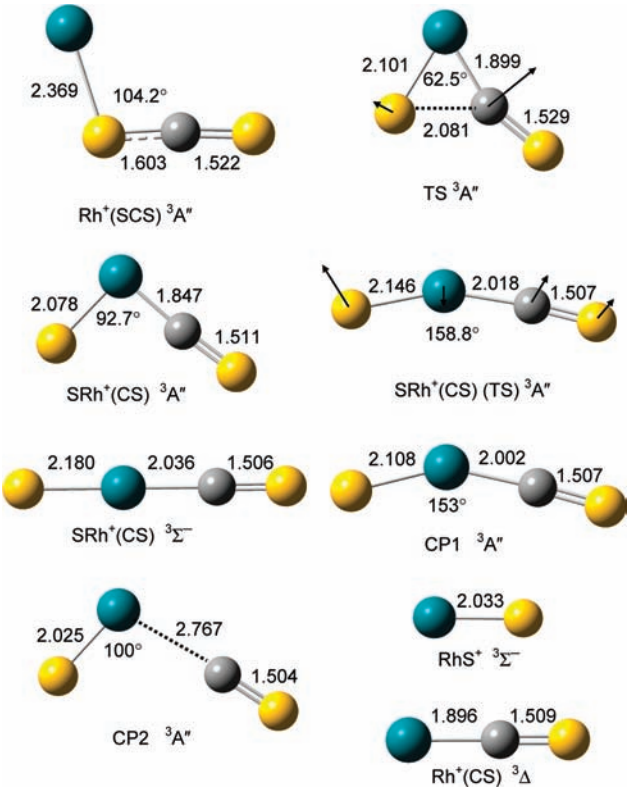

Figure 2. Triplet spin intermediates, crossing points, transition states, and products calculated at the B3LYP/Def2TZVPP level of theory. Bond lengths are shown in angstroms. All species are planar. Atoms are color coded: rhodium, blue; carbon, gray; and sulfur, yellow. Displacement vectors are shown for the imaginary frequency of the transition states.

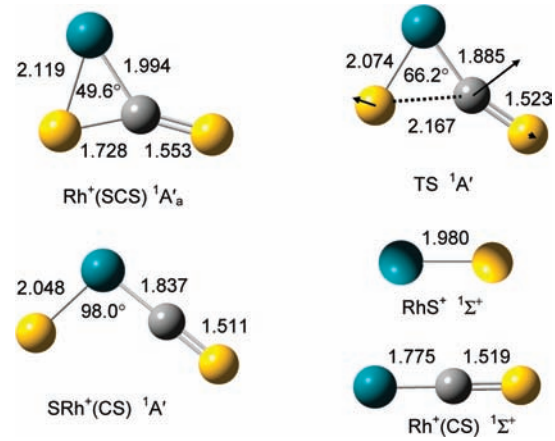

Figure 3. Singlet spin intermediates, transition states, and products calculated at the B3LYP/Def2TZVPP level of theory. Bond lengths are shown in angstroms. All species are planar. Atoms are color coded: rhodium, blue; carbon, gray; and sulfur, yellow. Displacement vectors are shown for the imaginary frequency of the transition states.

energies and structural parameters are provided in Table 3. All of the intermediates and transition states are planar.

The initial interaction of ground state Rh^+ (^3F) with CS_2 forms a complex where the metal ion binds to one of the sulfur atoms (Figure 2). Geometry optimizations started with linear RhSCS structures always collapsed to this bent geometry, which can be envisioned as the donation of electrons from the nonbonding π orbital of CS_2 into the empty 5s orbital on Rh. The ground state complex has A″ (C_s) symmetry where the CS bond attached to the Rh cation has extended to 1.603 Å from the

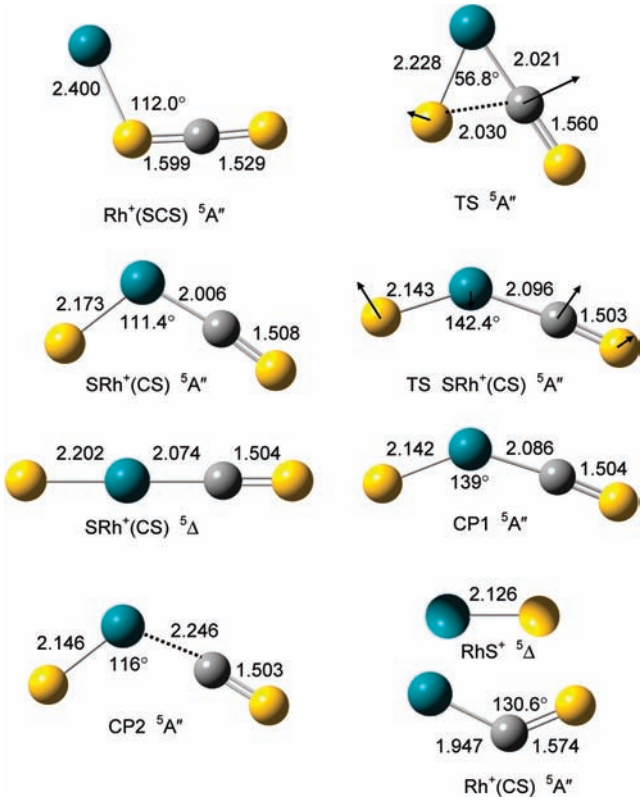

Figure 4. Quintet spin intermediates, crossing points, transition states, and products calculated at the B3LYP/Def2TZVPP level of theory. Bond lengths are shown in angstroms. All species are planar. Atoms are color coded: rhodium, blue; carbon, gray; and sulfur, yellow. Displacement vectors are shown for the imaginary frequency of the transition states.

1.553 Å value in free CS_2 as a result of the electron donation. This intermediate is bound by 1.23 eV relative to the $Rh^+(^3F) + CS_2$ reactants. Insertion of the metal ion into the CS bond takes place via the transition state TS($^3A''$). The imaginary frequency of 398 cm^{-1} corresponds to the expected elongation of the CS bond. The transition state has slightly longer RhS and RhC bond lengths and a smaller ∠SRhC bond angle compared to the $SRh^+(CS)$ ($^3A''$) intermediate that is formed next. Relaxed potential energy scans verify that the transition state connects the two adjacent intermediates. The $SRh^+(CS)$ intermediate has a slightly longer RhS bond compared to the $^3\Sigma^-$ state of the RhS^+ product and a slightly shorter RhC bond compared to the $^3\Delta$ state of the $Rh^+(CS)$ product (Figure 2). The intermediate can be viewed as donation of the σ(CS) lone pair of electrons (the HOMO) into the 3σ orbital of RhS^+ ($^3\Sigma^-$). The bent geometry permits a back-bonding interaction from a 1δ orbital of RhS^+ to CS, stabilizing the bent configuration compared to a linear geometry in which any such back-bonding interaction would share π electrons with the RhS bond. Consistently, a linear $^3\Sigma^-$ state of the $SRhCS^+$ intermediate is located 1.10 eV higher in energy and has longer RhS and RhC bonds (by 0.10 and 0.19 Å, respectively) than the bent intermediate (Figure 2). The transition state for conversion between the bent and linear intermediates is located at an SRhC bond angle of 159° and lies 0.20 eV *below* the linear intermediate at the CCSD(T) level (0.02 eV above at the B3LYP level where geometries are optimized). The potential energy surface at the B3LYP level for this conversion is shown in Figure 5a.

From either the bent or linear intermediates, cleavage of the metal ligand bonds can lead to both $RhS^+ + CS$ and $Rh^+(CS) + S$ product channels. If spin is conserved, the accessible product channel for reaction 1 is RhS^+ ($^3\Sigma^-$) + CS ($^1\Sigma^+$), which is an excited state for this channel (Table 1). For reaction 2, the situation is less clear-cut because of the triplet spin of the sulfur atom product. Adiabatically, the $SRh^+(CS)$ ($^3A''$) ground state intermediate correlates with the $Rh^+(CS)$ ($^3\Delta$) + S (^3P) ground state products; however, formation of $Rh^+(CS)$ ($^1\Sigma^+$) + S (^3P) and $Rh^+(CS)$ ($^5A''$) + S (^3P) are also spin-conserving.

Along the singlet surface, the reaction proceeds in a parallel fashion to the triplet surface (Figure 1). Here the intermediates and transition state have $^1A'$ symmetry. An end-on encounter complex, $Rh^+(SCS)$ ($^1A'_b$), similar to that along the triplet surface is located at 1.29 eV below the $Rh^+(^1G) + CS_2$ asymptote, comparable to the 1.23 eV bond energy for $Rh^+(SCS)$ ($^3A''$). However, lying 1.10 eV lower in energy is the $^1A'_a$ state having a geometry in which the metal cation clearly interacts with both a sulfur and the carbon atom (Figure 3). The CS bond being activated is much longer than for free CS_2, 1.728 versus 1.553 Å, and the SCS bond angle is now 152.8°. At the TS, the Rh−S and RhC bonds shorten, the CS bond continues to elongate, and the ∠SRhC angle increases as the metal inserts. These trends continue until the $SRh^+(CS)$ intermediate is formed. The imaginary frequency of 302 cm^{-1} corresponds to the expected motion, and the connection between both intermediates and the TS are confirmed by relaxed potential energy surface scans. The $SRh^+(CS)$ intermediate has a longer RhS bond than the $^1\Sigma^+$ state of the RhS^+ product and a longer RhC bond than the $^1\Sigma^+$ state of the $Rh^+(CS)$ product (Figure 3). As for the triplet state, this intermediate is formed by donation of the σ(CS) lone pair of electrons into the empty 3σ orbital of RhS^+ ($^1\Sigma^+$). Again the bent geometry is favored because it allows back-donation from the 1δ orbital of RhS^+ to the CS π^* orbitals. A linear singlet $SRh^+(CS)$ intermediate is located 1.57 eV higher in energy and has imaginary frequencies such that it collapses to the bent species. From the bent intermediate, spin-conserving cleavage of the metal ligand bonds can lead to RhS^+ ($^1\Sigma^+$) + CS ($^1\Sigma^+$), which is an excited state for this channel (Table 1). Adiabatically, the $^1A'$ state of the $SRh^+(CS)$ intermediate correlates with the ground state $Rh^+(CS)$ ($^3\Delta$) + S (^3P) asymptote, but spin is also conserved to form $Rh^+(CS)$ ($^1\Sigma^+$) + S (^3P).

The quintet surface is distinct from the lower spin surfaces. The initial interaction between $Rh^+(^5F)$ and CS_2 is much less attractive (Figure 1) but forms an $Rh^+(SCS)$ intermediate comparable in geometry to the triplet ground state (Figure 4). The energy required to move from $Rh^+(SCS)$ ($^5A''$) to the insertion TS is only 0.13 eV, comparable to the barrier height for the singlet surface (0.07 eV) but much lower than for the ground state triplet (0.69 eV). The quintet transition state has RhS and RhC bond lengths that are much longer than those in the triplet and singlet states (Figures 2−4). Similar trends are observed for the $^5A''$ state of the $SRh^+(CS)$ intermediate compared to its lower spin counterparts. Also in contrast to the low-spin counterparts, the linear form of the $SRh^+(CS)$ intermediate, a $^5\Delta$ state, is comparable in energy to the bent form (0.28 and 0.22 eV below GS reactants, respectively). Whereas the bent intermediate has an ∠SRhC bond angle of 111°, the transition state connecting it to the linear form has an angle of 142° and lies only 0.18 eV above the linear form (0.11 eV above the bent intermediate). The B3LYP potential energy surface connecting these species is shown in Figure 5b. Because of the high spin character, the stabilization gained by back-bonding interactions in the bent forms of the lower spin intermediates is mediated for the quintet state, such that the linear and bent forms have comparable energies (Figure 1). From either the $^5A''$

TABLE 3: Geometric Parameters, Vibrational Frequencies, and Relative Energies for Ground State Reactants and Products, and Intermediates and Transitions States for Reaction of Rh^+ with CS_2[a]

species	state	r(Rh−S), Å	r(Rh−C), Å	r(C−S), Å	∠RhSC or ∠SRhC, deg	∠SCS or ∠RhCS, deg	ν cm^{-1}	E_{rel}[b] eV
$Rh^+ + CS_2$	$^3F + {}^1\Sigma_g^+$			1.553 (2)		180.0[c]	408 (2), 678, 1561	0.00 (0.00)
Rh^+(SCS)	$^3A''$	2.369		1.603, 1.522	104.2[c]	175.5[c]	64, 230, 380, 415, 646, 1529	−1.23 (−1.38)
	$^1A'_a$	2.119	1.994	1.728, 1.553	61.4[c] 49.6[d]	152.8[c]	166, 350, 357, 424, 549, 1267	−0.69 (−0.34)
	$^1A'_b$	2.152		1.602, 1.533	156.4[c]	151.3[c]	57, 209, 218, 393, 704, 1423	0.42 (0.28)
	$^5A''$	2.400		1.599, 1.529	112.0[c]	176.8[c]	67, 162, 326, 355, 627, 1460	0.92 (0.63)
TS	$^3A''$	2.101	1.899	2.081, 1.529	54.0,[c] 62.5[d]	136.0,[c] 160.5[d]	−398, 182, 306, 354, 491, 1329	−0.55 (−0.56)
	$^1A'$	2.074	1.885	2.167, 1.523	52.7,[c] 66.2[d]	138.9,[c] 160.0[d]	−302, 203, 292, 380, 416, 1377	−0.49 (−0.10)
	$^5A''$	2.228	2.021	2.030, 1.560	56.4,[c] 56.8[d]	112.9,[c] 179.6[d]	−368, 152, 187, 223, 370, 1157	1.06 (0.97)
SRh^+(CS)	$^3A''$	2.078	1.847	1.511	92.7[d]	175.7[d]	102, 296, 324, 404, 478, 1432	−1.02 (−1.00)
	$^1A'$	2.048	1.837	1.511	98.0[d]	179.4[d]	98, 293, 347, 404, 516, 1441	−0.86 (−0.51)
	$^5\Delta$	2.202	2.074	1.504	180.0[d]	180.0[d]	66 (2), 249, 284 (2), 345, 1429	−0.28 (−0.24)
	$^5A''$	2.173	2.006	1.508	111.4[d]	173.0[d]	67, 211, 270, 387 (2), 1400	−0.22 (−0.18)
	$^5A''$ (CP2)	2.146	2.246	1.503	116[d]	174	47, 138, 214, 240, 414, 1408	−0.11 (−0.03)
	$^5A''$ (TS)	2.143	2.096	1.503	142.4[d]	174.7[d]	−112, 161, 212, 244, 418, 1418	−0.10 (−0.08)
	$^5A''$ (CP1)	2.142	2.086	1.504	139[d]	175[d]	−102, 167, 210, 246, 421, 1416	−0.10 (−0.08)
	$^3\Sigma^-$	2.180	2.036	1.506	180.0[d]	180.0[d]	43, 62, 246, 274, 298, 334, 1412	0.08 (−0.02)
	$^3A''$ (TS)	2.146	2.018	1.507	158.8[d]	175.0[d]	−102, 195, 257, 261, 361, 1407	−0.12 (0.00)
	$^3A''$ (CP1)	2.108	2.002	1.507	153[d]	177[d]	−231, 142, 234, 274, 395, 1407	0.10 (−0.02)
	$^3A''$ (CP2)	2.025	2.767	1.504	100[d]	179[d]	−122, 51, 191, 198, 534, 1402	0.70 (0.77)
	$^1\Sigma^+$	2.084	2.078	1.507	180.0[d]	180.0[d]	−910, −113, 108, 175, 250, 465, 1403	0.71 (1.00)
RhS^+ + CS	$^5\Delta + {}^1\Sigma^+$	2.126		1.532			427 1311	1.90 (1.91)
Rh^+(CS) + S	$^3\Delta + {}^3P$		1.896	1.509		180.0[d]	260 (2), 347, 1435	1.61 (1.71)

[a] Geometrical parameters calculated at the B3LYP/Def2TZVPP level of theory. [b] Relative energies calculated at CCSD(T)/Def2TZVPP//B3LYP/Def2TZVPP (B3LYP/Def2TZVPP) levels of theory, corrected for zero point energies. Absolute calculated energies for the ground state reactants are 943.506306 (944.806970) E_h, including zero point energies. [c] ∠RhSC and ∠SCS. [d] ∠SRhC and ∠RhCS.

or the $^5\Delta$ SRh^+(CS) intermediates, the ground state products of reaction 1, RhS^+ ($^5\Delta$) + CS ($^1\Sigma^+$), can be formed. Adiabatically, this intermediate again correlates with the ground state Rh^+(CS) ($^3\Delta$) + S (^{3}P) asymptote, but spin is also conserved to form Rh^+(CS) ($^5A''$) + S (^{3}P).

Triplet/Quintet Surface Crossing. As noted above, formation of the ground state products of reaction 1 from ground state reactants requires changing spin from triplet to quintet. The efficiency of this spin change will be influenced by the extent of spin−orbit coupling (enhanced by the presence of both the heavy metal and sulfur) as well as the character of the seam over which the two spin surfaces interact. To approximate the character of the crossing seam, we take the approach of Yoshizawa et al.[72] Thus, a relaxed potential energy surface scan at the B3LYP/Def2TZVPP level along a likely region of coordinate space for each spin state is conducted and then single point energies of the other spin state at the same geometries are also calculated. In this system, we examined both the region involving the SRhC bond angle as well as the dissociation coordinate, i.e., stretching the SRh^+−CS bond from both bent and linear intermediates.

The results of the relaxed potential energy surface scan calculations are shown in Figure 5. Geometries of the approximate crossing points (CPs) are shown in Figures 2 and 4, with their energies listed in Table 3. For the bending coordinate along the optimized triplet surface (Figure 5a), the crossing point (^{3}CP1) occurs just before the transition state at a ∠SRhC bond angle of ∼153°, r(Rh−C) = 2.00 Å, and an energy just above that of the reactants. Along the quintet surface (Figure 5b), ^{5}CP1 again lies just before the transition state at a bond angle of ∼139°, r(Rh−C) = 2.09 Å, and an energy just below that of the reactants. Given the shallowness of the potential energy surface along the bending angle (Figure 1), it seems likely that there is a fairly broad seam over which the two spin surfaces interact, all at energies well below the dissociation asymptote for either reaction 1 or 2.

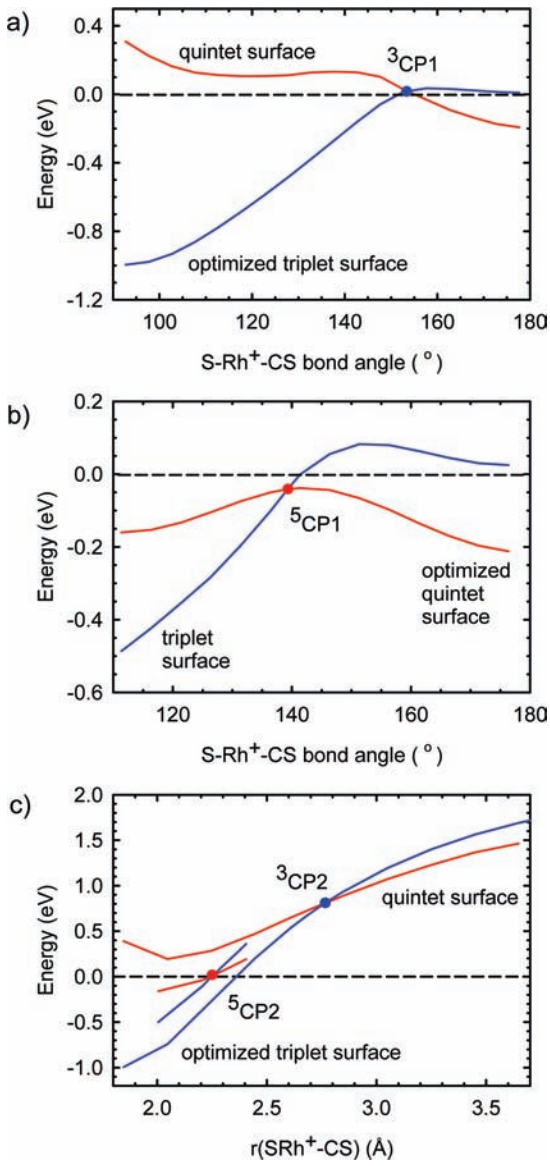

Figure 5. Relaxed potential energy surface scans at the B3LYP/Def2TZVPP level of theory for bending the $SRh^+(CS)$ intermediate (parts a and b) and for stretching the SRh^+-CS bond (part c). Results are shown for optimization along the triplet (parts a and c) and quintet (parts b and c) surfaces with single point energies at the same geometries for the other spin state. Approximate crossing points (CP) between the surfaces are also indicated. In part c, the optimized surface is the lower energy surface for both spin states.

When the reaction coordinate for SRh^+-CS bond dissociation is examined, we find that the linear intermediates do not cross at all (not shown in Figure 5), consistent with the fact that the linear quintet intermediate and the product asymptote are both lower than the triplet surface. For dissociation from the bent triplet intermediate (Figure 5c), ^{3}CP2 lies at $r(Rh-C) = 2.77$ Å, $\angle SRhC \sim 100°$, and an energy of 0.70 eV. Along the quintet state dissociation pathway (Figure 5c), ^{5}CP2 lies at $r(Rh-C) = 2.25$ Å, $\angle SRhC \sim 116°$, and an energy just below that of the reactants. Again, the seam for where these two spin surfaces interact appears to be extensive, with the crossing points lying well below the product asymptotes.

Experimental Results

Reaction of Rh^+ with CS_2 yields two major products, RhS^+ and $RhCS^+$, formed in reactions 1 and 2, as depicted in Figure 6. Both cross sections rise from similar apparent thresholds just below 2 eV, but clearly the $RhS^+ + CS$ products are strongly favored as the RhS^+ cross section rises rapidly with increasing energy, whereas the $RhCS^+ + S$ product cross section rises much more slowly. At higher energies, both cross sections decline more rapidly, which can be attributed to dissociation of the products in the overall process 6, which starts at $D_0(SC-S) = 4.50 \pm 0.04$ eV[70] for both channels.

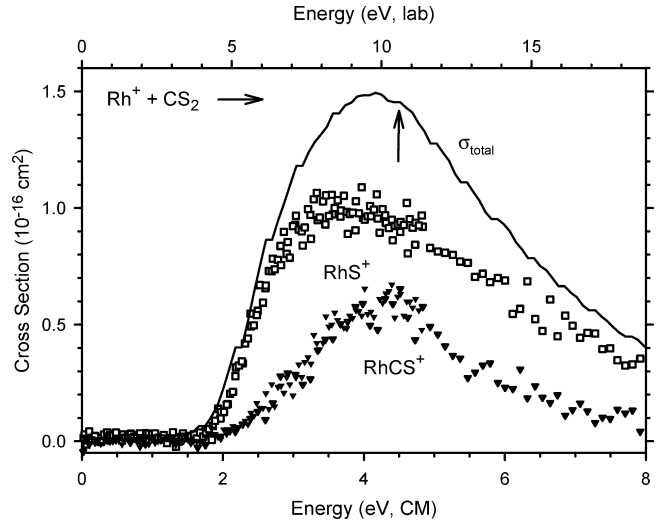

Figure 6. Product cross sections for the reaction of Rh^+ with CS_2 to form RhS^+ (open squares), $RhCS^+$ (closed inverted triangles), and their sum (line) as a function of center-of-mass energy (lower axis) and laboratory energy (upper axis). The arrow marks $D_0(S-CS) = 4.50$ eV.

$$Rh^+ + CS_2 \rightarrow Rh^+ + CS + S \qquad (6)$$

Note that the decline in the total and $RhCS^+$ cross sections starts close to this energy, in accord with this hypothesis. In contrast, the RhS^+ cross section actually reaches a maximum at somewhat lower energies, about 3.5 eV, and declines more slowly. The more rapid decline above the onset for reaction 6 in the $RhCS^+$ channel can be attributed to the atomic neutral product, which can only carry away energy in translational degrees of freedom, whereas the CS neutral product associated with the RhS^+ product ion can remove energy in rotations, vibrations, and translations.

The early maximum in the RhS^+ cross section is potentially attributable to competition with the $RhCS^+$ product at these higher energies, which is consistent with the total cross section exhibiting the expected behavior. Another possible reason for the early cross section decline is the spin multiplicities of the species involved in reaction 1, which is spin-forbidden to form ground state products, as discussed above. The effect of spin inversion on the cross-section shape has been demonstrated in a detailed study of the reaction of V^+ with CS_2.[73] Here the cross section of the VS^+ product reaches its maximum at even lower energies, a result that has been explained by consideration of the energy dependence of the surface-crossing probability for a spin-forbidden reaction. Specifically, more energetic reactants pass through the surface crossing region more rapidly, which reduces the ability of the electrons to adjust to different configurations along the reaction coordinate. Thus, a spin-forbidden path can exhibit a reaction efficiency that changes as $E^{-1/2}$, which can be included in the data analysis by using a value of 1.5 (instead of the usual 1.0) for the parameter m.

TABLE 4: Summary of Parameters in Eqs 3 and 4 Used To Analyze the Cross Sections for Reactions 1 and 2[a]

reaction	σ_0	n	m	E_0, eV	$D_0(Rh^+-X)$, eV
$Rh^+ + CS_2 \rightarrow$					
$RhS^+ + CS$	2.5(0.2)[b]	0.7(0.1)	1.0	2.17(0.09)	2.33(0.10)
	3.8(1.3)[b]	0.9(0.1)	1.5	2.11(0.12)	2.39(0.13)
	1.5(0.3)[c]	1.1(0.2)	1.0	1.89(0.09)	2.61(0.12)
	1.3(0.2)[c]	1.7(0.1)	1.5	1.88(0.09)	2.62(0.12)
	1.3(0.2)[d]	1.2(0.1)	1.0	1.89(0.08)	2.61(0.11)
	1.3(0.2)[d]	1.7(0.1)	1.5	1.88(0.08)	2.61(0.11)
$\rightarrow RhCS^+ + S$	1.2(0.1)[b]	1.2(0.1)	1.0	2.11(0.12)	2.39(0.13)
	1.9(0.03)[b]	1.4(0.1)	1.5	2.06(0.12)	2.44(0.13)
	6.2(1.6)[c,e]	1.1(0.2)	1.0	1.91(0.11)	2.59(0.13)
	5.8(1.2)[c,e]	1.7(0.1)	1.5	1.92(0.10)	2.58(0.13)
	58(15)[d,e]	1.2(0.1)	1.0	1.77(0.12)	2.73(0.14)
	57(14)[d,e]	1.7(0.1)	1.5	1.77(0.11)	2.73(0.13)

[a] Uncertainties are in parentheses. Values for E_0 are two standard deviations. [b] Single channel fit using eq 3. [c] Competitive fit using eq 4 with loose (PSL) transition states for both channels. [d] Competitive fit using eq 4 with a tight transition state for reaction 2. [e] Parameters assuming $^5\Delta$ product.

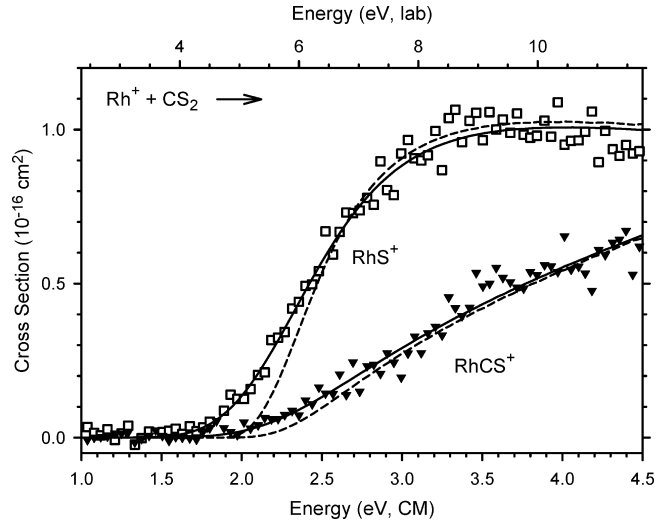

Figure 7. Cross sections for the reaction of Rh^+ with CS_2 to form RhS^+ (open squares) and $RhCS^+$ (closed inverted triangles) as a function of center-of-mass energy (lower axis) and laboratory energy (upper axis). Solid lines show the competitive model cross sections given by eq 4 with loose (PSL) TSs and the parameters given in Table 4 (m = 1.0). Dashed lines show these models in the absence of experimental kinetic energy distributions for reactants at 0 K.

However, even though reaction 1 is spin-forbidden to produce ground state RhS^+ ($^5\Delta$), it is spin-allowed to form the low-lying RhS^+ ($^3\Sigma^-$) excited state. The presence of a low-lying spin-allowed path may mean that the spin constraints are not severe in this reaction. Further, the extensive and low-energy triplet/quintet surface crossing seams may also permit facile spin inversion. For formation of the metal-thiocarbonyls in reaction 2, spin conservation is not an issue because the triplet spin of the atomic sulfur product, S (^{3}P), allows spin to be conserved for all states of $RhCS^+$.

Careful analysis of the threshold regions for the cross sections of reactions 1 and 2 using eq 3 yields the σ_0, n, and E_0 values summarized in Table 4 for m = 1.0 and 1.5. Analysis was performed by analyzing the reaction channels independently, in which case the values of n used to reproduce the data are distinct, ~0.8 and ~1.3, respectively. This result properly reflects the very different rates at which the RhS^+ and $RhCS^+$ cross sections rise from threshold. The threshold energies for the two channels are very similar, although somewhat surprisingly, that for reaction 2 is slightly lower (by ~0.05 eV), even though the $RhCS^+$ product is not favored. Use of m = 1.5 yields slightly lower threshold energies (by ~0.05 eV) for both channels compared to values obtained with m = 1.0. The high-energy regions of the cross sections are reproduced well using the correct onset energy for further dissociation, 4.50 eV = D_0(S−CS), and a simple model to account for the sequential dissociation.[74]

When these channels are analyzed as competitive reactions, eq 4 is able to reproduce the data nicely throughout the threshold region, up to 4.5 eV, where reaction 6 can begin. In the competitive analysis, the value of n used is the same for both channels and the EM is assumed to be the ground state SRh^+(CS) intermediate with an energy relative to the reactants calculated at the CCSD(T)//B3LYP level. Similarly good reproduction is obtained for both m = 1.0 and 1.5. Figure 7 shows an example of the competitive analysis with m = 1.0 and the average threshold energies listed in Table 4. Note that the shape of the RhS^+ cross section (specifically the maximum at about 3.5 eV) is well-reproduced; therefore, this behavior can be attributed to competition with formation of $RhCS^+$. Likewise the shape of the $RhCS^+$ cross section is also well-reproduced, even though it has a very different energy dependence than the RhS^+ cross section and the parameters n and m are the same for both channels. Because reaction 2 involves the cleavage of a covalent bond in the SRh^+(CS) intermediate, it is possible that this process is more accurately described by a tight transition state, as found elsewhere for such cleavages.[52,53] When the data are competitively modeled using the tightest conceivable transition state for this barrierless dissociation, we find that the reproduction of the data is virtually identical to that shown in Figure 7. The threshold energy for reaction 1 is essentially unchanged from the value obtained when both channels have PSL transition states, but that for reaction 2 drops by about 0.16 eV, consistent with a larger kinetic shift associated with the tight transition state.

In these competitive analyses, the thresholds for the two reactions are again very similar (Table 4), in accord with the appearance of the data. [Differences in the two thresholds are 0.02 ± 0.03 eV when m = 1.0 and 0.03 ± 0.03 eV when m = 1.5 for the loose (PSL) transition state assumption and 0.12 ± 0.03 and 0.11 ± 0.03 eV, respectively, for the tight TS assumption.] The competitive analysis thresholds are lower than those from the independent analysis because of the effects of competition with the channel leading back to reactants, the only available pathway at low energies. The competitive analysis demonstrates unambiguously that the main reason for the predominance of the $RhS^+ + CS$ channel over $RhCS^+ + S$ is the difference in the number of states available, because this channel has four rotational and two vibrational degrees of freedom, whereas the $RhCS^+ + S$ channel has only two rotations and four vibrations. Thus, the cross section for the former channel dominates the products, even though the relative energetics are virtually the same (PSL assumption) or even favor the latter channel (tight TS assumption). Indeed, if the competition between the two channels is calculated purely on the basis of the rovibrational degrees of freedom, the $RhCS^+ + S$ channel would be even smaller than shown in Figure 7. To reproduce the data, this channel needs to be scaled by a factor of 4.3 ± 0.7 (4.4 ± 0.7 for m = 1.5) when the RhS^+ product is assumed to have molecular parameters associated with the $^5\Delta$ ground state and loose PSL TSs are assumed (as reflected by the σ_0 values of Table 4). The needed scaling factor is rationalized by

TABLE 5: Experimental and Theoretical Bond Energies (eV)

bond	exp	B3LYP[a]	CCSD(T)//B3LYP[a]	CCSD(T)//CCD[a]	CCSD(T)[a]
Rh^+-S	2.61 ± 0.12	2.77 (2.79)	2.32 (2.45)	2.37 (2.47)	2.42 (2.54)
Rh^+-CS	2.66 ± 0.19	2.98 (2.99)	2.61 (2.74)	2.56 (2.69)	2.67 (2.80)
MAD[b]		0.24 ± 0.11	0.17 ± 0.17	0.17 ± 0.10	0.10 ± 0.13

[a] In all cases, theoretical values are obtained at the level shown using the Def2TZVPP basis set. Values are corrected for zero point energies and include counterpoise corrections for basis set superposition errors. Values in parentheses do not include counterpoise corrections. [b] Mean absolute deviation from experimental values.

accounting for the electronic degeneracies of the two channels. That for RhS^+ ($^5\Delta$) + CS ($^1\Sigma^+$) is lower than that for Rh^+(CS) ($^3\Delta$) + S (^{3}P), 10 versus 54, a factor of 5.4, in good agreement with the empirically found scaling factor. (These scaling factors rise to 42 ± 14 and 45 ± 14, respectively, when the tight TS is assumed for reaction 2. Such large factors are difficult to rationalize, suggesting that this TS is too tight.) The fact that one channel is spin-allowed and the other spin-forbidden may alter the effective scaling factor. In this regard, we also analyzed the data assuming that the spin-allowed RhS^+ ($^3\Sigma^-$) product is formed instead. The fitting parameters of eq 4 remain comparable to those obtained for the $^5\Delta$ state (thresholds for both channels drop by 0.02 eV), with the largest change being the scaling factor, which drops to 3.3 ± 0.7 (3.4 ± 0.7 for $m = 1.5$). This is because the vibrational frequency of RhS^+ ($^3\Sigma^-$) is 24% higher than that of RhS^+ ($^5\Delta$) (Table 1). For these products, the ratio of electronic degeneracies for reactions 1 and 2 is now 3 versus 54, or a factor of 18, substantially larger than the factor obtained experimentally. Finally, we note that the value of n used in these competitive fits is near unity when $m = 1.0$, a conventional line-of-centers value. When $m = 1.5$, the value of n rises by a comparable amount, 0.6, compensating for the change in the energy dependence. Overall, there is no clear indication that the extra value of $E^{-1/2}$ is needed, but the final threshold results are essentially independent of this parameter.

The E_0 values can be converted to Rh^+-S and Rh^+-CS bond strengths at 0 K using eq 7, where X represents either S or CS. The D_0 values are also provided in Table 4.

$$D_0(Rh^+-X) = D_0(SC-S) - E_0 \qquad (7)$$

It can be seen that the values obtained from the competitive modeling are within experimental uncertainty of the independent analyses, where preliminary versions of the latter have been reported previously.[30] We believe that the more sophisticated competitive modeling, which reproduces both cross sections simultaneously, provides the most accurate threshold values in addition to being more precise. Although there are indications that the tight TS may be too tight, a conservative measure of these bond energies averages the results from both the loose (PSL) and tight TS assumptions. We conservatively take the average of the competitive fits using $m = 1.0$ and 1.5 and both loose (PSL) and tight transition state assumptions for reaction 2. Thus, our final values are $D_0(Rh^+-S) = 2.61 \pm 0.12$ eV and $D_0(Rh^+-CS) = 2.66 \pm 0.19$ eV, where the uncertainties are two standard deviations. (If results from the tight TS assumption are not included, the former value is unchanged and the latter value becomes 2.59 ± 0.13 eV.) Uncertainties include variations among the TS assumptions and values of m, multiple data sets (seven), frequencies of reactants and products ($\pm 10\%$), time available for reaction (factor of 2 in $\tau = 5 \times 10^{-4}$ s), absolute energy of the EM (± 0.3 eV), and the uncertainty in the absolute zero of energy (± 0.02 eV). Values outside these conservative uncertainties are not able to reproduce the data well.

Discussion

Thermochemistry. Including corrections for basis set superposition errors in the full counterpoise limit, the calculated bond energy of the RhS^+ ($^5\Delta$) ground state is 2.77 eV at the B3LYP level of theory, considerably higher than the 2.32, 2.37, and 2.42 eV values calculated at the CCSD(T)//B3LYP, CCSD(T)//CCD, and CCSD(T) levels of theory, respectively (Table 5). All these values are in reasonable agreement with the experimental bond energy of 2.61 ± 0.12 eV, with discrepancies comparable to those of the calibration calculations for the CCSD(T) levels. Because of spin-conservation in the exit channel, as noted above and further examined below, it is possible that the experimental threshold corresponds to formation of the RhS^+ ($^3\Sigma^-$) excited state. After counterpoise corrections, the RhS^+ ($^3\Sigma^-$) species has calculated bond energies of 2.41 eV (B3LYP), 2.16 eV (CCSD(T)//B3LYP), 2.03 eV (CCSD(T)//CCD), and 2.07 eV (CCSD(T)). All of these theoretical values are now outside of experimental uncertainty. On the basis of these comparisons, we conclude that spin need not be conserved in reaction 1.

For the rhodium thiocarbonyl cation, the $^3\Delta$ ground state is bound by 2.98, 2.61, 2.56, and 2.67 eV at the B3LYP, CCSD(T)/B3LYP, CCSD(T)/CCD, and CCSD(T) levels of theory, respectively, including counterpoise corrections[75,76] (Table 5). The CCSD(T) values are in excellent agreement with the experimental value of 2.66 ± 0.16 eV. Here, there are no spin restrictions in the formation of any of the $RhCS^+$ states. Note that theory indicates that the Rh^+-CS bond is stronger than the Rh^+-S bond by 0.20−0.29 eV (Table 5), whereas experiment finds differences from −0.03 to 0.12 eV (Table 4). However, the metal−ligand bonding in these two molecules is quite distinct, covalent for RhS^+ and dative for $RhCS^+$, such that theory may not provide balanced views of both interactions.

It should also be noted that the spin−orbit interactions in these product ions may differ appreciably. Experimental bond energies refer to the ground spin−orbit state at 0.00 eV, $^3F_4$ for Rh^+. In contrast, calculations are referenced to the statistically weighted mean of all spin−orbit levels in the ground state term, 0.20 eV for Rh^+ (^{3}F).[63] Because our calculations do not explicitly include spin−orbit interactions, it is possible that calculated bond energies should be reduced by this different asymptotic energy before comparison with experimental values. However, spin−orbit effects influence the energetics of all reactants, intermediates, and products with unknown and varying magnitudes. For instance, recent spectroscopic studies of $RhS(^4\Sigma^-)$ find a small spin−orbit splitting of 47.43 cm^{-1} (0.0059 eV) between the $\Omega = 3/2$ and 1/2 states.[19] However, given the uncertainties, we do not apply corrections in the present work, which implicitly assumes that the spin−orbit corrections largely cancel.

Reaction Mechanism. The reaction coordinate diagram of Figure 1 shows clearly that reactions 1 and 2 occur by insertion of the rhodium cation into a CS bond of CS_2 followed by simple cleavage of one of the metal ligand bonds. The experimental results correspond to reaction of ground state $Rh^+(^3F)$, which the calculations indicate can form the ground state $Rh^+(CS)$ ($^3\Delta$) + S (^3P) products by remaining on the triplet surface throughout the reaction. In contrast, formation of the ground state RhS^+ ($^5\Delta$) + CS ($^1\Sigma$) products clearly requires a change in spin. The calculations shown in Figure 5 indicate that the spin change can occur along the bending coordinate in the $SRh^+(CS)$ intermediate or in the exit channel as the SRh^+-CS bond is broken. Because these calculations suggest that the surface crossing seams are fairly extensive and relatively low in energy, it seems likely that the spin−orbit coupling between the quintet and triplet surfaces is relatively strong and, therefore, that our experimental threshold for reaction 1 corresponds to the formation of ground state RhS^+ ($^5\Delta$) product ion. This conclusion is consistent with the fact that theory [at the CCSD(T) level] and experiment agree well regarding the RhS^+ bond energies for the $^5\Delta$ ground state.

Summary

The gas-phase reactivity of atomic rhodium cations with carbon disulfide has been investigated with guided-ion-beam mass spectrometry. Careful analysis and evaluation of the threshold energies, reactivities, and cross sections results in bond dissociation energies of $D_0(Rh^+-S) = 2.61 \pm 0.12$ eV and $D_0(Rh^+-CS) = 2.66 \pm 0.19$ eV. The values are in good agreement with theoretical calculations at the CCSD(T)/Def2TZVPP//B3LYP/Def2TZVPP and CCSD(T)/Def2TZVPP//CCD/Def2TZVPP levels of theory, whereas B3LYP/Def2TZVPP calculations tend to overbind. The potential energy surfaces for both processes clearly indicate that the mechanism involves insertion of the metal ion into a CS bond, followed by elimination of one of the two ligands. Coupling between surfaces of triplet and quintet spin appears to be efficient, in part because these surfaces cross at several places in the vicinity of the $SRh^+(CS)$ insertion intermediate.

Note Added in Proof. We inadvertently omitted mention of the previous flow tube studies of Bohme and coworkers,[77] who examined the reactions of atomic cations of rhodium with carbon disulfide, CS_2, at room temperature in a high pressure of He. They observed only $Rh^+(CS_2)$ adduct formation. These results are consistent with the endothermic reaction observed in the present work. Unlike the studies of Bohme and coworkers,[77] no $Rh^+(CS_2)$ adducts are observed at low energies in our work because the single collision conditions used here do not allow the collisional relaxation necessary to form such adducts.

Acknowledgment. Profs. D. Schröder and H. Schwarz are thanked for their support and guidance when these data were taken. This work was supported by the Fonds der Chemischen Industrie (graduate fellowship for I.K.) and the National Science Foundation (P.B.A., CHE-0748790). In addition, we thank the Center for High Performance Computing at the University of Utah for a generous allocation of computer time.

References and Notes

(1) (a) Fărcasiu, D.; Ghenciu, A.; Li, J. Q. *J. Catal.* **1996**, *158*, 116. (b) Allali, N.; Prouzet, E.; Michalowicz, A.; Gaborit, V.; Nadiri, A.; Danot, M. *Appl. Catal., A* **1997**, *159*, 333. (c) Mdleleni, M. M.; Hyeon, T.; Suslick, K. S. *J. Am. Chem. Soc.* **1998**, *120*, 6189. (d) Dos Santos, A. C. B.; Grange, P.; Faro, A. C., Jr. *Appl. Catal., A* **1999**, *178*, 29. (e) Janssens, J.-P.; van Langeveld, D. A.; Moulijn, J. A. *Appl. Catal., A* **1999**, *179*, 229.

(2) Raje, A. P.; Liaw, S.-J.; Srinivasan, R.; Davis, B. H. *Appl. Catal., A* **1997**, *150*, 297–318.

(3) For a comparison of hydrodechlorination and hydrodesulfurization selectivities and activities of MS (M = V−Ni; Mo−Pd, W, Ir, Pt), see: Frimmel, J.; Zaradzil, M. *J. Catal.* **1997**, *167*, 286.

(4) Eijsbouts, S.; De Beer, V. H. J.; Prins, P. *J. Catal.* **1988**, *109*, 217.

(5) Afanasiev, P.; Bezverkhyy, I. *Appl. Catal., A* **2007**, *322*, 129–141.

(6) Daudin, A.; Brunet, S.; Perot, G.; Raybaud, P.; Bouchy, C. *J. Catal.* **2007**, *248*, 111–119.

(7) Dowell, F. S.; Greenfield, H. *J. Am. Chem. Soc.* **1965**, *87*, 2767.

(8) Yamada, M.; Koizum, N.; Miyazawa, A.; Furukawa, T. *Catal. Lett.* **2002**, *78*, 195–199.

(9) Gulla, A. F.; Gancs, L.; Allen, R. J.; Mukerjee, S. *Appl. Catal., A* **2007**, *326*, 227–235.

(10) Ziegelbauer, J. M.; Gatewood, D.; Gulla, A. F.; Guinel, M. J.-F.; Ernst, F.; Ramaker, D. E.; Mukerjee, S. *J. Phys. Chem. C* **2009**, *113*, 6955–6968.

(11) Jin, C.; Xia, W.; Nagaiah, T. C.; Guo, J.; Chen, X.; Bron, M.; Schuhmann, W.; Muhler, M. *Electrochim. Acta* **2009**, in press.

(12) Zhang, W.; Yanagisawa, K.; Kamiya, S.; Shou, T. *Crystal Growth Design* **2009**, *9*, 3765–3770.

(13) Zhang, W. X.; Yanagisawa, K.; Kamiya, S.; Shou, T. *Chem. Lett.* **2009**, *38*, 210–211.

(14) Sosibo, N. M.; Revprasadu, N. *Mater. Sci. Eng., B* **2008**, *150*, 111–115.

(15) Rufus, B.; Ramakrishnan, V.; Viswanathan, B.; Kuriacose, J. C. *Langmuir* **1990**, *6*, 565–567.

(16) Gilchrist, R.; Wichers, E. *J. Am. Chem. Soc.* **2002**, *57*, 2565.

(17) Wichers, E. *J. Am. Chem. Soc.* **2002**, *46*, 1818.

(18) Suc, N. V. *J. Radioanal. Nucl. Chem.* **1994**, *187*, 67–71.

(19) Li, R.; Balfour, W. J.; Hopkins, W. S.; Adam, A. G. *J. Mol. Spectrosc.* **2005**, *234*, 211–215.

(20) Kretzschmar, I.; Schröder, D.; Schwarz, H.; Rue, C.; Armentrout, P. B. *J. Phys. Chem. A* **1998**, *102*, 10060–10073.

(21) Rue, C.; Armentrout, P. B.; Kretzschmar, I.; Schröder, D.; Harvey, J. N.; Schwarz, H. *J. Chem. Phys.* **1999**, *110*, 7858–7870.

(22) Schröder, D.; Kretzschmar, I.; Schwarz, H.; Rue, C.; Armentrout, P. B. *Inorg. Chem.* **1999**, *38*, 3474–3480.

(23) Bärsch, S.; Kretzschmar, I.; Schröder, D.; Schwarz, H.; Armentrout, P. B. *J. Phys. Chem. A* **1999**, *103*, 5925–5934.

(24) Kretzschmar, I.; Schröder, D.; Schwarz, H.; Rue, C.; Armentrout, P. B. *J. Phys. Chem. A* **2000**, *104*, 5046–5058.

(25) Kretzschmar, I.; Schröder, D.; Schwarz, H. *J. Phys. Chem. A* **2001**, *105*, 8456–8464.

(26) Rue, C.; Armentrout, P. B.; Kretzschmar, I.; Schröder, D.; Schwarz, H. *Int. J. Mass Spectrom.* **2001**, *210/211*, 283–301.

(27) Rue, C.; Armentrout, P. B.; Kretzschmar, I.; Schröder, D.; Schwarz, H. *J. Phys. Chem. A* **2002**, *106*, 9788–9797.

(28) Kretzschmar, I. Schr̈; oder, D.; Schwarz, H.; Armentrout, P. B. *Int. J. Mass Spectrom.* **2003**, *228*, 439–456.

(29) Kretzschmar, I.; Schröder, D.; Schwarz, H.; Armentrout, P. B. *Int. J. Mass Spectrom.* **2006**, *249−250*, 263–278.

(30) Kretzschmar, I.; Schröder, D.; Schwarz, H.; Armentrout, P. B. *Advances in Metal and Semiconductor Clusters*; Duncan, M. A., Ed.; 2001, Vol. 5, pp 347−394.

(31) Armentrout, P. B.; Kretzschmar, I. Work in progress.

(32) Armentrout, P. B.; Kretzschmar, I. *Inorg. Chem.* Submitted.

(33) Armentrout, P. B.; Kretzschmar, I. *J. Chem. Phys.* Submitted.

(34) Ervin, K. M.; Armentrout, P. B. *J. Chem. Phys.* **1985**, *83*, 166.

(35) Schultz, R. H.; Armentrout, P. B. *Int. J. Mass Spectrom. Ion Processes* **1991**, *107*, 29.

(36) Chen, Y.-M.; Elkind, J. L.; Armentrout, P. B. *J. Phys. Chem.* **1995**, *99*, 10438–10445.

(37) Chen, Y.-M.; Armentrout, P. B. *J. Chem. Phys.* **1995**, *103*, 618–625.

(38) Chen, Y.-M.; Armentrout, P. B. *J. Phys. Chem.* **1995**, *99*, 10775–10779.

(39) Chen, Y.-M.; Armentrout, P. B. *J. Am. Chem. Soc.* **1995**, *117*, 9291–9304.

(40) Gerlich, D. *Adv. Chem. Phys.* **1992**, *82*, 1–176.

(41) Chesnavich, W. J.; Bowers, M. T. *J. Phys. Chem.* **1979**, *83*, 900–905.

(42) Aristov, N.; Armentrout, P. B. *J. Am. Chem. Soc.* **1986**, *108*, 1806–1819.

(43) Schultz, R. H.; Crellin, K. C.; Armentrout, P. B. *J. Am. Chem. Soc.* **1991**, *113*, 8590.

(44) Armentrout, P. B. In *Advances in Gas Phase Ion Chemistry*; Adams, N. G., Babcock, L. M., Eds.; JAI Press: Greenwich, 1992; Vol. 1, pp 83−119.

(45) Armentrout, P. B. *Int. J. Mass Spectrom.* **2000**, *200*, 219–241.

(46) Herzberg, G. *Molecular Spectra and Molecular Structure*; Van Nostrand Reinhold: New York, 1966; Vol. III.
(47) Rodgers, M. T.; Ervin, K. M.; Armentrout, P. B. *J. Chem. Phys.* **1997**, *106*, 4499.
(48) Rodgers, M. T.; Armentrout, P. B. *J. Chem. Phys.* **1998**, *109*, 1787.
(49) Gilbert, R. G.; Smith, S. C. *Theory of Unimolecular and Recombination Reactions*; Blackwell Scientific: London, 1990.
(50) Truhlar, D. G.; Garrett, B. C.; Klippenstein, S. J. *J. Phys. Chem.* **1996**, *100*, 12771.
(51) Holbrook, K. A.; Pilling, M. J.; Robertson, S. H. *Unimolecular Reactions*, 2nd ed.; Wiley: New York, 1996.
(52) Muntean, F.; Heumann, L.; Armentrout, P. B. *J. Chem. Phys.* **2002**, *116*, 5593.
(53) Muntean, F.; Armentrout, P. B. *J. Phys. Chem. A.* **2003**, *107*, 7413.
(54) The ADF package is available: te Velde, G.; Baerends, E. J. Dept. Theoretical Chemistry, Vrije Universiteit, Amsterdam, The Netherlands.
(55) Snijders, J. G.; Baerends, E. *J. Mol. Phys.* **1977**, *33*, 1651.
(56) Vosko, S. H.; Wilk, L.; Nusair, M. *Can. J. Phys.* **1980**, *58*, 1200.
(57) Becke, A. D. *Phys. Rev. A* **1988**, *38*, 3098.
(58) Perdew, J. P. *Phys. Rev. B* **1986**, *33*, 8822.
(59) Levy, M.; Perdew, J. P. *Int. J. Quantum Chem.* **1994**, *49*, 539.
(60) Frisch, M. J.; Trucks, G. W.; Schlegel, H. B.; Scuseria, G. E.; Robb, M. A.; Cheeseman, J. R.; Montgomery, J. J. A.; Vreven, T.; Kudin, K. N.; Burant, J. C.; Millam, J. M.; Iyengar, S. S.; Tomasi, J.; Barone, V.; Mennucci, B.; Cossi, M.; Scalmani, G.; Rega, N.; Petersson, G. A.; Nakatsuji, H.; Hada, M.; Ehara, M.; Toyota, K.; Fukuda, R.; Hasegawa, J.; Ishida, M.; Nakajima, T.; Honda, Y.; Kitao, O.; Nakai, H.; Klene, M.; Li, X.; Knox, J. E.; Hratchian, H. P.; Cross, J. B.; Adamo, C.; Jaramillo, J.; Gomperts, R.; Stratmann, R. E.; Yazyev, O.; Austin, A. J.; Cammi, R.; Pomelli, C.; Ochterski, J. W.; Ayala, P. Y.; Morokuma, K.; Voth, G. A.; Salvador, P.; Dannenberg, J. J.; Zakrzewski, V. G.; Dapprich, S.; Daniels, A. D.; Strain, M. C.; Farkas, O.; Malick, D. K.; Rabuck, A. D.; Raghavachari, K.; Foresman, J. B.; Ortiz, J. V.; Cui, Q.; Baboul, A. G.; Clifford, S.; Cioslowski, J.; Stefanov, B. B.; Liu, G.; Liashenko, A.; Piskorz, P.; Komaromi, I.; Martin, R. L.; Fox, D. J.; Keith, T.; Al-Laham, M. A.; Peng, C. Y.; Nanayakkara, A.; Challacombe, M.; Gill, P. M. W.; Johnson, B.; Chen, W.; Wong, M. W.; Gonzalez, C.; Pople, J. A. *Gaussian 03, Revision B.02*; Gaussian, Inc.: Pittsburgh, PA, 2003.
(61) Becke, A. D. *J. Chem. Phys.* **1993**, *98*, 5648–5652.
(62) Lee, C.; Yang, W.; Parr, R. G. *Phys. Rev. B* **1988**, *37*, 785–789.
(63) Eichkorn, K.; Weigend, F.; Treutler, O.; Ahlrichs, R. *Theor. Chem. Acc.* **1997**, *97*, 119.
(64) Weigend, F.; Ahlrichs, R. *Phys. Chem. Chem. Phys.* **2005**, *7*, 3297.
(65) Andrae, D.; Haeussermann, U.; Dolg, M.; Stoll, H.; Preuss, H. *Theor. Chim. Acta* **1990**, *77*, 123–141.
(66) Feller, D. *J. Comput. Chem.* **1996**, *17*, 1571–1586.
(67) Schuchardt, K. L.; Didier, B. T.; Elsethagen, T.; Sun, L.; Gurumoorthi, V.; Chase, J.; Li, J.; Windus, T. L. *J. Chem. Inf. Model.* **2007**, *47*, 1045.
(68) Cizek, J. *Adv. Chem. Phys.* **1969**, *14*, 35–89.
(69) Purvis, G. D. I.; Bartlett, R. J. *J. Chem. Phys.* **1982**, *76*, 1910.
(70) Prinslow, D. A.; Armentrout, P. B. *J. Chem. Phys.* **1991**, *94*, 3563.
(71) Sancho, F. J. *Anales Real. Soc. Esp. Fis. Quim.* **1958**, *54A*, 41.
(72) Yoshizawa, K.; Shiota, Y.; Yamabe, T. *J. Chem. Phys.* **1999**, *111*, 538–545.
(73) See reference 21.
(74) Weber, M. E.; Elkind, J. L.; Armentrout, P. B. *J. Chem. Phys.* **1986**, *84*, 1521.
(75) Boys, S. F.; Bernardi, R. *Mol. Phys.* **1970**, *19*, 553.
(76) van Duijneveldt, F. B.; van Duijneveldt de Rijdt, J. G. C. M.; van Lenthe, J. H. *Chem. Rev.* **1994**, *94*, 1873.
(77) Cheng, P.; Koyanagi, G. K.; Bohme, D. K. *J. Phys. Chem. A* **2006**, *110*, 2718–2728.

JP907253R